General theory of three-dimensional radiance measurements with optical microprobes

N. Fukshansky-Kazarinova, L. Fukshansky, M. Kühl, and B. B. Jørgensen

Measurements of the radiance distribution and fluence rate within turbid samples with fiber-optic radiance microprobes contain a large variable instrumental error caused by the nonuniform directional sensitivity of the microprobes. A general theory of three-dimensional radiance measurements is presented that provides correction for this error by using the independently obtained function of the angular sensitivity of the microprobes. © 1997 Optical Society of America

Key words: Optics of living tissue; radiance measurements; fiber-optic microprobe; three-dimensional picture of a light field in turbid media.

1. Introduction

Studies of light-controlled processes in photomedicine, photobiology, and ecology require a detailed knowledge of the light microenvironment within absorbing turbid media such as living tissue and sediments. Direct three-dimensional measurements of radiation fields in such samples with optical fiber microprobes have been increasingly employed over the past several years.[1–9]

The most universal type of optical fiber probe is the radiance microprobe, which has a tip diameter as small as 10 μm and a directional sensitivity mainly concentrated around the axis of the probe within a solid angle as small as 10°. In contrast to other types that sense the entire spherical or hemispherical flux,[8] it is the only probe that provides the angular distribution of radiance. A radiance distribution at a given depth is found on the basis of successive measurements with a radiance microprobe advanced to this depth in different zenithal directions, θ, relative to the light source as shown in Fig. 1. The unit sphere containing all directions (Fig. 1) is subdivided into K spherical bands, and within each band i one measurement under the angle θ_i is carried out. This measurement is representative for the radiance in any direction within the band number i, i.e., the radiance within each band is assumed to be constant. We designate this radiance value as L_i. To the accuracy of this discretization the solid radiance distribution is given by the sequence of measured values L_i: $L(\theta) = \{L_1, L_2, \ldots, L_k\}$.

The fluence rate $I(P)$ in a point P (see Fig. 1) is then obtained as a sum of L_i weighted with the fractional areas of the corresponding spherical bands, w_i:

$$I(P) = 2\pi \int_{\theta} L(\theta) d\theta \approx 4\pi \sum_{i=1}^{K} L_i w_i \tag{1}$$

The weighting factors w_i are easily derived from the geometrical considerations as

$$w_i = (\cos\bar{\theta}_{i-1} - \cos\bar{\theta}_i)/2,$$
$$\bar{\theta}_0 = 0, \bar{\theta}_K = \pi, \qquad \sum_i w_i = 1,$$

where $\bar{\theta}_{i-1}$, $\bar{\theta}_i$ are the zenithal angles for the boundary circles on the unit sphere delimiting the band i (see Fig. 1). Importantly, a measurement in this scheme in principle yields not the radiance L_i but the radiant flux $L_i S$, where S is the reference area of the microprobe on the unit sphere (S is shown as a bright circle in Fig. 1). Thus the reading of a measurement should be divided by S to obtain L_i.

However, as shown elsewhere,[10] the described measurements produce erroneous values of L_i. This intrinsic instrumental error results from the nonuniform angular sensitivity of the microprobe.

Radiance microprobes (for technical details see Refs. 2, 4, and 6) have well-defined light-collecting

L. Fukshansky is with the Department of Biology, University of Freiburg, Schanzlestrausse 1, D-79104 Freiburg, Germany. The other authors are with the Max Planck Institute of Marine Microbiology, Microsensor Research Group, Celsiusstrausse 1, D-28359 Bremen, Germany.

Received 24 April 1996; revised manuscript received 5 December 1996.
0003-6935/97/256520-09$10.00/0

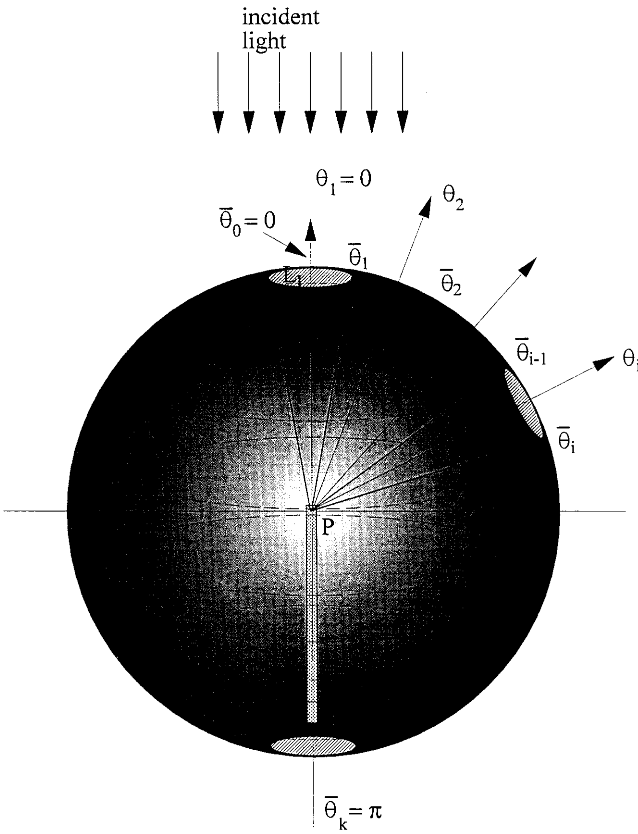

Fig. 1. Spatial design of three-dimensional radiance measurements. To perform the measurement number i, the microprobe advanced to the point P is oriented in the direction θ_i ($i = 1, 2, \ldots, K$). Each measurement is representative of the radiance within the corresponding spherical band of the unit sphere circumscribing the point P. The radiance value L_i is assumed to be constant within the band number i. $\bar{\theta}_{i-1}$, $\bar{\theta}_i$ are the zenithal angles of the circles delimiting the band i.

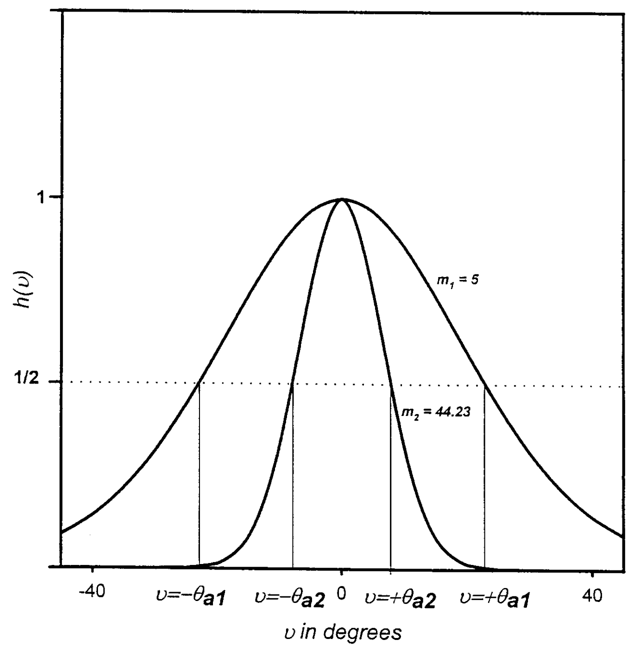

Fig. 2. Angular sensitivity distribution of a microprobe: υ is the internal angular coordinate; $\upsilon = 0$ concides with the axis of the probe; $h(\upsilon)$ is the relative sensitivity [see Eq. (2)], $h(\upsilon)$ is maximal for $\upsilon = 0$ while light deviating from the axis is perceived with lower sensitivity. The acceptance half-angle $\pm\theta_a$ specifies the υ values for which $h(\upsilon) = 0.5\ h_{\max}$. Function $h(\upsilon)$ is specified for a concrete probe by fixing either parameter m or angle θ_a. The two curves represent a flat ($m_1 = 5$; $\theta_{a1} = 21.2°$) and a strongly peaked ($m_2 = 44.23$; $\theta_{a2} = 7.2°$) sensitivity distribution.

properties. The directional sensitivity of a radiance microprobe is specified by a numerical aperture $n_0 \sin(\theta_a)$, where n_0 is the refraction index of the medium and θ_a is the acceptance half-angle of the optical fiber.[11] The meaning of θ_a is clear from Fig. 2, which shows examples of the angular sensitivity distribution of a probe h as a function of the deviation υ from the optical axis of the probe. The sensitivity $h(\upsilon)$, being maximal along the axis of the probe, decreases monotonously with υ. The angle θ_a specifies such deviation υ for which $h(\upsilon) = 0.5h_{\max}$. The bell-shaped distribution $h(\upsilon)$ is directly measurable. It can be approximated by a slightly modified Gaussian formula:[10]

$$h(\upsilon) = \cos(\upsilon)\exp[-m \sin^2(\upsilon)], \tag{2}$$

where the fitting coefficient m adjusts the function to the individual curve of the microprobe under consideration. Parameters m and θ_a are related as

$$m = \ln(2 \cos \theta_a)/\sin^2 \theta_a.$$

Figure 2 shows two functions $h(\upsilon)$, with $m = 44.23(\theta_a = 7.2°)$ and $m = 5(\theta_a = 21.2°)$. Both Eq. (2) and Fig. 2 present the normalized function $h(\upsilon)$, i.e., $h_{\max} = 1$.

If a probe with the sensitivity distribution $h(\upsilon)$ such as that in Fig. 2 is used to measure L_i in the scheme shown in Fig. 1, its optical axis has the orientation θ_i, thus providing $\upsilon = 0$ for $\theta = \theta_i$. Only the radiance directed exactly along θ_i is perceived with maximal sensitivity. The sensitivity for those radiances L_i that belong to the band i (e.g., with $\bar{\theta}_{i-1} < \theta < \bar{\theta}_i$) but deviate from the direction θ_i is decreasing with increasing deviation from θ_i, as prescribed by the function $h(\upsilon)$. Furthermore, the probe also senses radiances from the neighboring bands. Thus any single measurement produces not the average radiance within the targeted band but a linear combination of different radiances weighted by the function $h(\upsilon)$. This measured quantity, which we designate as M_i, deviates from L_i.

In a recent paper[10] we reported on the first step toward the analysis of the instrumental error and stated the problem of theoretical correction of the measurements. The idea of this approach was to process the measured data by using additional information contained in the function $h(\upsilon)$ that is measured independently. We developed this theory for the special case of equidistant measurements and accounted for the distorting contributions of only two immediate neighbors (i.e., bands $i - 1$ and $i + 1$).

In this paper the general theory for arbitrarily spaced measurements is presented. In Subsection 2.A the problem is formulated in mathematical terms and the basic system of linear equations connecting L_i and M_i is derived. The coefficients of the equations are surface integrals of $h(\upsilon)$, with the complicated domains of integration arising from the geometry of measurements. Subsection 2.B contains an elucidation of these domains that is the prerequisite for the solution of the integrals given in Subsection 2.C. In Subsection 2.D we consider an application of the theory to our measurements in a costal sediment with diatoms. This treatment yields the instrumental error for the measured radiance distribution and fluence rate. It also shows that the divergent measured values obtained on the same sample with different probes converge very well after they were treated by the correcting procedure.

2. Results

A. Mathematical Formulation of the Problem

Let us consider radiation in an arbitrary point P within a turbid sample illuminated from above as shown in Fig. 1. Introducing spherical coordinates θ (zenith angle) and Ψ (azimuth angle) associated with the unit sphere circumscribing P, we assume that at any point (θ, Ψ) the radiance depends on θ but not on Ψ. As described in Section 1, K measurements with a microprobe having the directional sensitivity distribution $h(\upsilon)$ are performed in the point P in the directions θ_i:

$$0 \leq \theta_1 < \theta_2 \cdots < \theta_K \leq \pi.$$

The results of these measurements are designated $M_i (i = 1, 2, \ldots, K)$. The unit sphere is subdivided into K spherical bands (see Section 1), and radiance within each band is assumed to have a constant value $L_i (i = 1, 2, \ldots, K)$. The circles delimiting these bands are described by equations $\theta = \bar{\theta}_j (j = 1, 2, \ldots, K - 1)$, where $\bar{\theta}_j$ can be chosen arbitrarily within a set that obeys the inequality

$$\theta_i < \bar{\theta}_i < \theta_{i+1}, \quad \bar{\theta}_0 = 0, \quad \bar{\theta}_K = \pi.$$

The zenithal distribution of radiance thus appears as a stepwise constant function:

$$L(\theta) = L_i \qquad \text{for} \qquad \bar{\theta}_{i-1} \leq \theta < \bar{\theta}_i \quad (i = 1, 2, \ldots K)$$

(compare Fig. 1). The problem is to calculate all L_i on the basis of the measured quantities $M_i (i = 1, 2, \ldots, K)$ and known function $h(\upsilon)$.

For an individual measurement under zenith angle $\theta = \theta_i \leq \pi/2$, we introduce local Cartesian coordinates x, y, z and also corresponding spherical coordinates υ, ψ associated with the point P and direction θ_i, so that $\upsilon = \theta - \theta_i$ (see Fig. 3). The angular sensitivity of the measurement, $h(\upsilon)$, is defined on the whole hemisphere

$$\textstyle\sum_i: (0 \leq \upsilon \leq \pi/2, \qquad 0 \leq \psi \leq 2\pi)$$

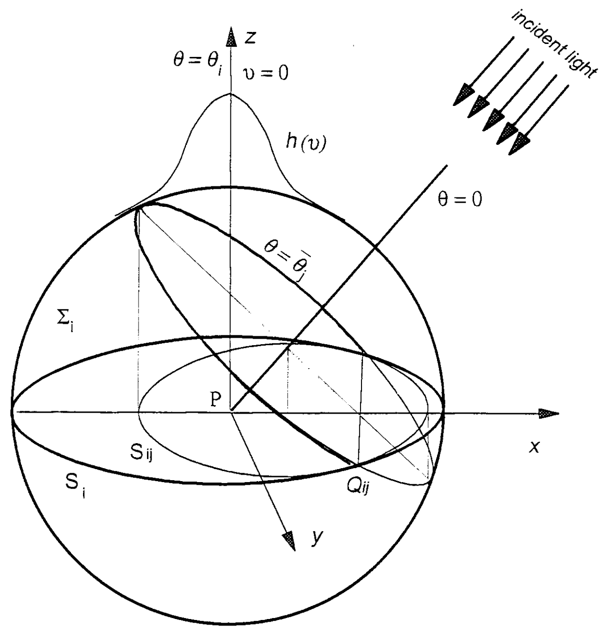

Fig. 3. Geometry of a single measurement in the $\theta = \theta_i$ direction. The incident light comes from the $\theta = 0$ direction, which is the same as in Fig. 1; however, here the picture is turned clockwise on θ_i. x, y, z is the Cartesian coordinate system associated with this measurement. Σ_i is the hemisphere of the unit sphere seen from the $\theta = \theta_i$ direction. S_i is the circumference of radius 1 centered at point P; it is also a projection of the boundary of Σ_i onto the plane xPy. Ellipse S_{ij} is a projection of the delimiting circle $\theta = \bar{\theta}_j$ (cf. Fig. 1) onto the plane xPy. Q_{ij} is the point of contact of S_{ij} with S_i, υ is the zenithal spherical coordinate associated with the measurement in the $\theta = \theta_i$ direction, and $h(\upsilon)$ is the function of the angular sensitivity of the probe.

visible from the direction θ_i. As described above, the hemisphere Σ_i is subdivided into a set of spherical bands Σ_{ij} with constant radiance values L_j. Thus the magnitude M_i obtained in this measurement contains contributions from different parts of the hemisphere Σ_i:

$$M_i = \iint_{\Sigma_i} L(\theta) h(\upsilon) \mathrm{d}\Sigma = \sum_{j=1}^{n_i} L_j \iint_{\Sigma_{ij}} h(\upsilon) \mathrm{d}\Sigma = \sum_{j=1}^{n_i} L_i J_{ij} \tag{3}$$

with

$$J_{ij} = \iint_{\Sigma_{ij}} h(\upsilon) d\Sigma, \tag{4}$$

where n_i is the number of spherical bands contributing to the hemisphere Σ_i.

The system of linear equations, Eq. (3), contains K equations with K unknown variables L_j. Its coefficients J_{ij} can be estimated because $h(\upsilon)$ is a known function. Thus the system (3) provides a solution to our problem. However, the estimation of J_{ij} requires a major effort because the domains of integrations in Eq. (4) are complicated functions of all θ_i and $\bar{\theta}_j$, i.e., of the entire geometry of measurements. In

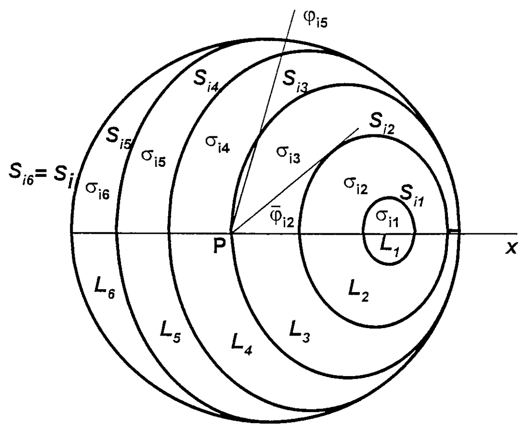

Fig. 4. Mapping of the spherical surface Σ_i onto the plane xPy performed for the measurement in the $\theta = \theta_i$ direction. Circumference S_i is the projection of the boundary of the hemisphere Σ_i onto the plane xPy. Ellipses S_{ij} are the projections of circles $\theta = \bar{\theta}_j$ onto plane xPy. The plane areas σ_{ij} are projections of spherical bands Σ_{ij} onto plane xPy; the index i means only that the mapping is performed within the geometry induced by the ith measurement. L_j is the radiance within the band Σ_{ij}. $\bar{\varphi}_{i2}$ is the polar coordinate of the point of tangency for a tangent drawn from point P to ellipse S_{i2}; φ_{i5} is the polar coordinate of the point of contact of ellipse S_{i5} with the circumference S_i.

the Subsection 2.B we analyze this geometry in order to facilitate the solution of the integrals J_{ij}.

B. Geometry of the Surface Integrals J_{ij}

Our starting point is the general relation between the integral of a function f over an arbitrary convex surface Σ and that over the plane σ:

$$\iint_{\Sigma} f(M)\mathrm{d}\Sigma = \iint_{\sigma} \frac{f(N)}{\cos(n, n_0)}\, \mathrm{d}\sigma, \tag{5}$$

where (n, n_0) is the angle between the normal to Σ in a point M and the normal to the plane σ, N is the projection of point M onto the plane, and $f(M) = f(N)$.

To calculate the integrals in Eq. (4) we map the spherical surface Σ_i onto the plane xPy (see Fig. 3). In this case we have $(n, n_0) = \upsilon$, the zenithal spherical coordinate of the local coordinate system associated with the ith measurement; $\Sigma = \Sigma_i$, the visible hemisphere corresponding to the ith measurement; and $\sigma = \sigma_i$, the circular disk bounded by the circumfernce S_i of radius 1 centered at point P.

The mapping transfers the delimiting circles $\theta = \bar{\theta}_j$ into ellipses S_{ij} and the surface areas Σ_{ij} into the plane areas σ_{ij} (compare Figs. 3 and 4). On the basis of formulas (4) and (5) we obtain

$$J_{ij} = \iint_{\sigma_{ij}} \frac{h(\upsilon)}{\cos(\upsilon)}\, \mathrm{d}\sigma. \tag{6}$$

Let us consider projections of the areas Σ_{ij} and their boundaries $\theta = \bar{\theta}_j$ onto the plane xPy. We are not interested in the circles $\theta = \bar{\theta}_j$ ($\bar{\theta}_j \leq \theta_i + \pi/2$) located completely outside the hemisphere Σ_i and consider only circles that belong to Σ_i either completely or partially. In the first case the corresponding ellipses S_{ij} are located completely inside the circular disk σ_i. In the second case they contact the circumference S_i in the points Q_{ij} (cf. Figs. 3 and 4), and we are interested only in the parts corresponding to those parts of the circles $\theta = \bar{\theta}_j$ which are located on the hemisphere Σ_i. We can also restrict the following consideration to the values $\theta_i \leq \pi/2$ because the case $\pi/2 < \theta_i \leq \pi$ is transferred to the case $\theta_i \leq \pi/2$ by the coordinate transformation $\theta' = \pi - \theta$. Thus the admissible domain of values of $(\theta_i, \bar{\theta}_j)$ under consideration is ($\theta_i < \pi/2$; $\bar{\theta}_j < \theta_i + \pi/2$), which is illustrated in Fig. 5. Also, the sum limit n_i in formula (3) can be easily estimated: it is equal to the maximal value of j, satisfying the inequality (see Fig. 3)

$$\bar{\theta}_j \geq \theta_i + \pi/2.$$

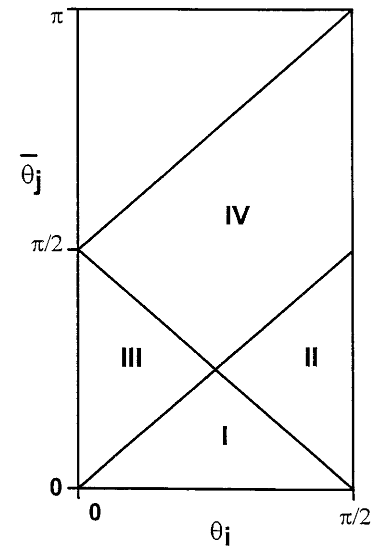

Fig. 5. Admissible domain of values of $(\theta_i, \bar{\theta}_j)$, subdivided into four subdomains with a specific relationship between θ_i and $\bar{\theta}_j$ in each one.

It is more convenient to consider within the circular disk σ_i a set of nested domains $\bar{\sigma}_{ij}$,

$$\bar{\sigma}_{i1} \subset \bar{\sigma}_{i2} \subset \cdots \subset \bar{\sigma}_{in_i} = \sigma_i,$$

instead of the set of nonoverlapping domains σ_{ij}. Each domain $\bar{\sigma}_{ij}$ is the internal area of the ellipse S_{ij} if this ellipse has no points of contact to S_i. Otherwise the domain $\bar{\sigma}_{ij}$ is circumferenced by the part of the ellipse S_{ij} contained between its points of contact Q_{ij}, Q_{ij}' to the circumference S_i and that part of S_i located between Q_{ij} and Q_{ij}' that is convex toward the positive direction of the axis x (see Fig. 4).

Let us introduce the integrals over the nested domains:

$$\bar{J}_{ij} = \iint_{\bar{\sigma}_{ij}} \frac{h(\upsilon)}{\cos(\upsilon)}\, \mathrm{d}\sigma. \tag{7}$$

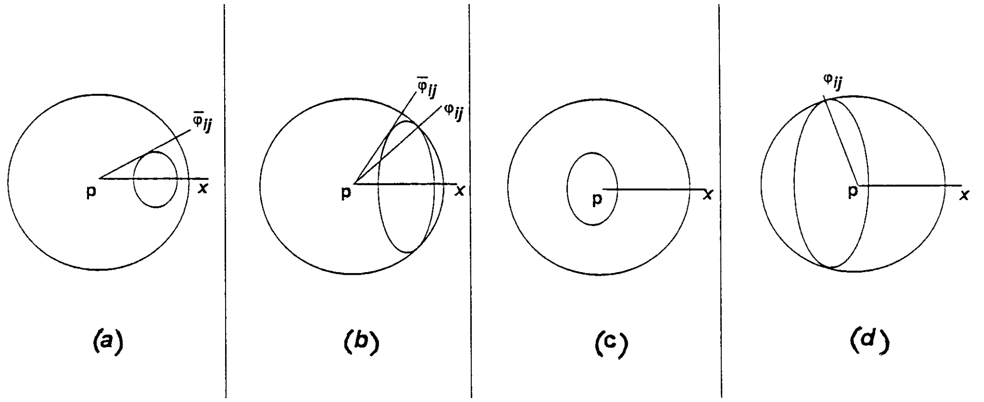

Fig. 6. Different positions of an ellipse S_{ij} with respect to the point P and circumference S_i on plane xPy as implied by the parameter θ_i, $\bar{\theta}_j$ representing the geometry of measurements. (a)–(d) correspond to θ_i, $\bar{\theta}_j$ values from domains I–IV in Fig. 5.

Obviously

$$J_{ij} = \bar{J}_{ij} - \bar{J}_{ij-1}\ (j = 1, 2, \ldots, n_i), \tag{8}$$

where (cf. Fig. 4)

$$\bar{J}_{i0} = 0, \qquad \bar{J}_{in_i} = 2\pi \int_0^1 \frac{h(\upsilon)}{\cos \upsilon} r\mathrm{d}r.$$

Thus the integrals J_{ij} can be easily calculated from integrals $\bar{J}_{ij}$ that have much more convenient integration domains. However, prior to this the limits of the surface integrals should be analytically derived. This derivation and the subsequent calculation of $\bar{J}_{ij}$ are given in Subsection 2.C.

C. Calculation of Integrals $\bar{J}_{ij}$

For the integration limits to be derived, the boundaries of the domains $\bar{\sigma}_{ij}$ should be described. We introduce polar coordinates r, φ (note that $r = \sin \upsilon$) on the plane xPy and also the double-valued function

$$f_{ij}^{\pm}(\varphi) = \frac{\cos \bar{\theta}_j \sin \theta_i \cos \varphi \pm \cos \theta_i [\sin(\theta_i + \theta_j)\sin(\theta_j - \theta_i) + \sin^2 \theta_i \cos^2 \varphi]^{1/2}}{\cos^2 \theta_i + \sin^2 \theta_i \cos^2 \varphi}, \tag{9}$$

which will be useful for the description of the ellipses S_{ij}.

An ellipse S_{ij} contains the coordinates origin P when the parameters θ_i, $\bar{\theta}_j$ satisfy the inequality

$$\sin(\theta_i + \bar{\theta}_j)\sin(\theta_i - \bar{\theta}_j) < 0,$$

i.e., $\theta_i < \bar{\theta}_j < \pi - \theta_i$. In this case its equation is presented by the single-valued function $r = f_{ij}^{+}(\varphi)$ (for the proof see Appendix A). Otherwise point P is located outside the ellipses S_{ij}. In such a case a tangent line from point P to the ellipse is always feasible. We designate the φ coordinate of the point of tangency as $\bar{\varphi}_{ij}$ (cf. Fig. 4).

If the ellipse is located completely within the positive semiaxis x (which takes place for $\bar{\theta}_j < \theta_i$), then to any value $0 < \varphi < \bar{\varphi}_{ij}$ correspond two values of r: $r = f_{ij}^{-}(\varphi)$ and $r = f_{ij}^{+}(\varphi)$. In this case the point of tangency is located on the boundary of a domain $\bar{\sigma}_{ij}$ and

$$\cos \bar{\varphi}_{ij} = \frac{[\sin(\theta_i + \theta_j)\sin(\theta_i - \theta_j)]^{1/2}}{\sin \theta_i}. \tag{10}$$

If $\bar{\theta}_j > \theta_i$ then the ellipse S_{ij} is located within the negative semiaxis x. In this case only the branch $r = f_{ij}^{+}(\varphi)$ makes a part of the boundary of $\bar{\sigma}_{ij}$ and the point of tangency is not located on the boundary.

The important boundary point for integration to be performed is the point of contact for an ellipse S_{ij} with the circumference S_{ij}. If such a point exists it is always located, as one can easily see, on a positive branch $r = f_{ij}^{+}(\varphi)$. The φ coordinate of this point we designate as φ_{ij}. The value of φ_{ij} is determined through the parameters θ_i, $\bar{\theta}_j$ as (see Appendix A)

$$\cos \varphi_{ij} = \cos \bar{\theta}_j / \sin \theta_i. \tag{11}$$

On the basis of the above considerations, four different cases appear with respect to the subdivision of the integration domain for an integral $\bar{J}_{ij}$ and elucidation of the integration limits in each subdomain. Accordingly, the admissible domain of parameters θ_i, $\bar{\theta}_j$ is subdivided into four subdomains, shown in Fig. 5. Below we consider all four cases and derive explicite formulas for $\bar{J}_{ij}$ in each case.

Case I. $\bar{\theta}_j < \theta_i$, $\bar{\theta}_j \le \pi/2 - \theta_i$. Ellipse S_{ij} is located completely on the positive semiaxis x and has no points of contact with S_i (or the unique point of contact has coordinate $\varphi_{ij} = 0$). This case is depicted in Fig. 6(a).

$$\bar{J}_{ij} = 2 \int_0^{\bar{\varphi}_{ij}} \mathrm{d}\varphi \int_{f_{ij}^{+}(\varphi)}^{f_{ij}^{-}(\varphi)} \frac{h(\upsilon)}{\cos(\upsilon)} r dr. \tag{12a}$$

Case II. $\bar{\theta}_j < \theta_i, \bar{\theta}_j > \pi/2 - \theta_i$. The ellipse S_{ij} is located on the positive semiaxis x and has the point of contact $\varphi_{ij} \neq 0$ with S_i [see Fig. 6(b)].

$$\bar{J}_{ij} = 2 \int_0^{\varphi_{ij}} \mathrm{d}\varphi \int_{f_{ij}^-(\varphi)}^{1} \frac{h(\upsilon)}{\cos(\upsilon)} r\mathrm{d}r + 2 \int_{\varphi_{ij}}^{\bar{\varphi}_{ij}} \mathrm{d}\varphi \int_{f_{ij}^-(\varphi)}^{f_{ij}^+(\varphi)} \frac{h(\upsilon)}{\cos(\upsilon)} r\mathrm{d}r. \tag{12b}$$

Case III. $\bar{\theta}_j > \theta_i, \bar{\theta}_j \leq \pi/2 - \theta_i$. Point P is located inside the ellipse S_{ij}, which has no point of contact with S_i [or the unique point of contact has coordinate $\varphi_{ij} = 0$; see Fig. 6(c)].

$$\bar{J}_{ij} = 2 \int_0^{\pi} \mathrm{d}\varphi \int_0^{f_{ij}^+(\varphi)} \frac{h(\upsilon)}{\cos(\upsilon)} r\mathrm{d}r. \tag{12c}$$

Case IV. $\bar{\theta}_j > \theta_i, \bar{\theta}_j > \pi/2 - \theta_i$. Ellipse S_{ij} is located completely or partially on the negative semiaxis x and has points of contact $\pm\varphi_{ij} \neq 0$ [see Fig. 6(d)].

$$\bar{J}_{ij} = 2 \int_0^{\pi} \mathrm{d}\varphi \int_0^{1} \frac{h(\upsilon)}{\cos(\upsilon)} r\mathrm{d}r - 2 \int_{\varphi_{ij}}^{\pi} \mathrm{d}\varphi \int_{f_{ij}^+(\upsilon)}^{1} \frac{h(\upsilon)}{\cos(\upsilon)} r\mathrm{d}r. \tag{12d}$$

Substituting Eq. (2) for $h(\upsilon)$ into Eqs. (12) and noting that $r = \sin \upsilon$, we can easily obtain a general solution for the internal integral in formulas (12):

$$\int_{f_1(\varphi)}^{f_2(\varphi)} \exp(-mr^2) r\mathrm{d}r = \frac{1}{2m} \{ \exp[-m f_1^{\,2}(\varphi)] - \exp[-m f_2^{\,2}(\varphi)] \}.$$

Thus for any set of θ_i, $\bar{\theta}_j$ presenting a concrete geometry of measurements and for a given m presenting the directional sensitivity of the concrete microprobe, integrals (12) and then [using Eq. (8)] integrals (4) can be calculated. Substituting integrals (4) into Eq. (3) and solving these equations with respect to $L_i (i = 1, 2, \ldots, K)$, one obtains the real radiances from the measured quantites M_i.

Note that when the measured radiation field contains a strong collimated component, for example, under illumination with a laser, the calculation of integrals J_{i1} can be developed in a special way involving the description of the collimated component as a singularity by means of δ functions. This appears to be necessary when the measurements are planed and discussed in the framework of the theory of radiative transfer, in which the collimated component is aways separated as a singularity. The appropriate procedure for the calculation of J_{i1} is given in Appendix B.

D. Example of Application: Correction of the Measurements and Stability of the Correcting Procedure

Here the theory is applied to our radiance measurements in costal sediments with diatoms. Proceeding from a true radiance distribution, solid $L(\theta)$, and corresponding fluence rate $I(\mathrm{P}) = \int L(\theta)\mathrm{d}\theta$, we find estimates of $L(\theta)$ and $I(P)$ (a) as the raw experimental data and (b) as the data processed by the theory, and then we compare estimates (a) and (b) one to another and to the true magnitudes. Furthermore, we repeat this procedure for probes with four different acceptance angles θ_a as well as for different angular distances between the measurements in order to reveal the effect of these characteristics on both processed and nonprocessed data.

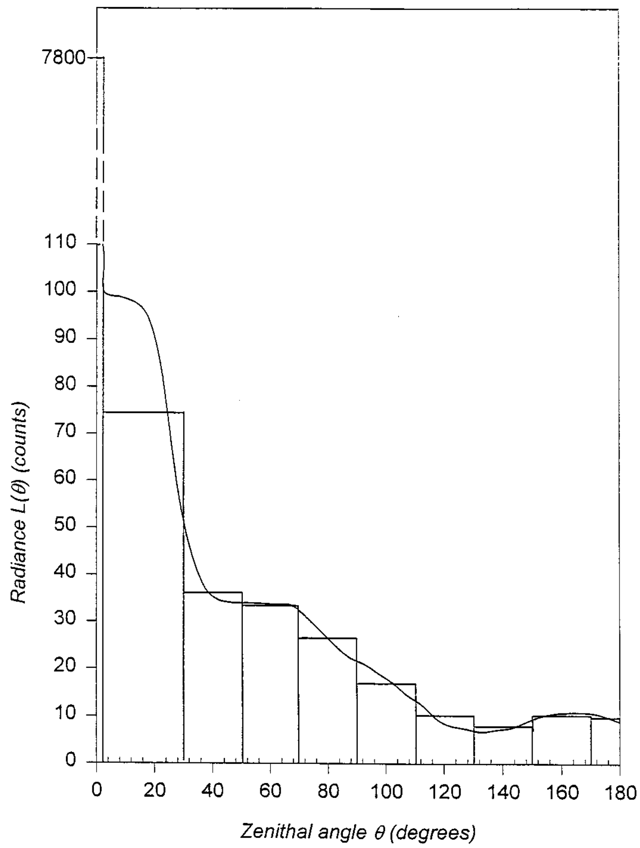

Fig. 7. True radiance distribution $L(\theta)$. This distribution with the fluence rate value of $I(P) = 349.9$ relative units is the starting point for the analysis of the correcting procedure. Averaged values $\bar{L}_i$ for spherical bands (specified by vertical lines) calculated on the basis of this distribution are used in Table 1.

We start with the true radiance distribution $L(\theta)$ shown in Fig. 7. Its diffuse part is a continuous function; the collimated part we interpret as a constant level radiance concentrated in the narrow angular range (0, 2.5°). The fluence rate of this radiation $I(\theta) = 349.9$ relative units.[12] On the basis of known $L(\theta)$, the measurable quantity $M(\theta)$ can be calculated for any direction θ_i and any microprobe as

$$\iint_{\Sigma_i} L(\theta) h(\theta - \theta_i) \mathrm{d}\Sigma = M_i. \tag{13}$$

This quantity calculated for four different m values is shown in Fig. 8. Because of a very extended range of values of $M(\theta)$, the angular domain near $\theta = 0°$ is

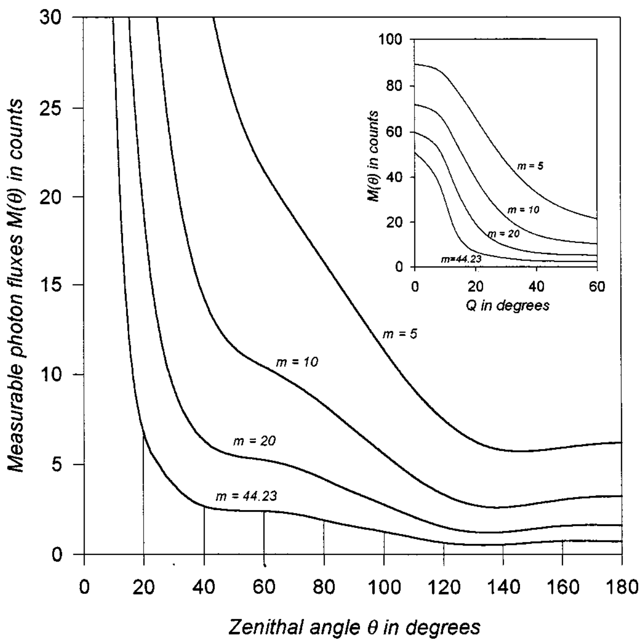

Fig. 8. Zenithal distributions of the measurable photon fluxes $M(\theta)$ based on the true radiance distribution $L(\theta)$ as they can be obtained by four microprobes with a different parameter m. Specified points of $\theta_i = 0°, 20°, 40°, \ldots, 180°$ were used to perform the correction procedure. The initial part of the curves $M(\theta)$ for the lower θ range is shown in the inset.

Table 1. Radiance Values L_i Recovered by Means of the Correcting Procedure Applied to the Measured Fluxes M_i from the Curves in Fig. 8[a]

Band No.	Band Range (deg)	$\bar{L}_i$	L_i Values			
			$m = 44.23$	$m = 20$	$m = 10$	$m = 5$
1	0–2.5	7800	8034	8229	8371	8186
2	2.5–30	74.5	78.1	77.7	76.7	80.7
3	30–50	36.1	34.3	32.8	31.9	26.6
4	50–70	33.5	33.9	34.5	35.6	42.0
5	70–90	25.4	25.4	25.5	25.0	29.0
6	90–110	16.8	16.7	16.6	16.8	20.7
7	110–130	8.5	8.0	7.8	7.8	4.6
8	130–150	8.0	7.8	7.7	7.7	10.0
9	150–170	10.7	10.9	11.1	11.2	9.1
10	170–180	9.6	9.7	9.5	9.0	14.8

[a]For each of four curves representing different microprobes, the M_i values corresponding to the ten equidistant points θ_i with the 20° step (0°, 20° . . . , 180°) were used. $\bar{L}_i$ is the true mean value as shown in Fig. 7.

shown separately in the inset at a different scale. On each curve in Fig. 8 one can read the fluxes (ordinate) measured by the corresponding microprobe oriented in the direction θ (abscissa) when the true distribution solid of radiance is presented by the function $L(\theta)$ from Fig. 7. Of course, the real measurements are performed only on a restricted number of points, providing an approximative shape of the curves in Fig. 8. For example, the measurements spaced equidistantly with the 20° step and performed with the probe having $m = 44.23$ are specified in Fig. 8. A comparison of the curves in Figs. 7 and 8 shows that the nonprocessed measurements give a severely distorted picture of the radiance distribution solid, especially those with larger acceptance angles of the probes. Only the probe with the most peaked directional sensitivity (Fig. 8, lowest curve) conveys more or less the shape of $L(\theta)$, although this is rather distorted and has strongly underestimated values.

Now let us process these data according to the theory. We consider the set of equidistant measurements with the 20° step in ten directions θ_i (0°, 20°, . . . , 180°) for all four probes, represented in Fig. 8. We subdivide the unit sphere into ten spherical bands with assumed constant radiance value L_i within each band. The numbers and zenithal areas of these bands are given in columns 1 and 2 of Table 1. Note that the first band is very narrow because we assume that the light within this zenithal area contains the nonscattered part of the incident collimated flux and can strongly differ from the surroundings. Then we perform the entire correcting procedure to find the L_i from the M_i. The results for the four probes are given in columns 4 to 7 of Table 1. These results should be compared with the true radiance values $L(\theta)$ averaged over each band, presented in column 3 of Table 1 as $\bar{L}_i$. Figure 7 shows the averaged true values $\bar{L}_i$ on the background of the radiance distribution $L(\theta)$. As one can see from Table 1, the correcting procedure recovers the radiance distribution solid with extremely high accuracy. The relative deviation of L_i from $\bar{L}_i$ is in almost all cases within $\pm 5\%$.

Let us address the estimates of the fluence rate $I(P)$ that are presented in Table 2. Column 1 contains the parameters of the four probes under consideration. Columns 2–4 contain the characteristics of the equidistant measurements constructed in accordance with each probe. For example, the probe with $\theta_a = 7.2°$ implies the step $\Delta = 15°$ between measurements. Correspondingly, the number of measurements is $K = 2\pi/\Delta + 1 = 13$. The reference area of a microprobe (see Section 1) for this band size is $S = 0.0538$. Note that the rather artificial magnitude S is necessary only for nonprocessed calculations to proceed from the measured flux M_i to the radiance L_i. In the framework of the theory, there is no place for the notion of S because the reference area is the entire hemisphere Σ_i and the transmission from the measured fluxes M_i to the radiance L_i is accomplished automatically through the integration and solution of system (3). Column 5 contains the results provided by the measurements characterized in columns 2–4. All these numbers strongly overestimate the true value $I(P) = 349.9$ presented above. In order to see the effect of deviations of the band size from the probe acceptance angle, we performed calculations with the fixed band size (20°) and corresponding number of measurements (ten) for different probes (column 6). The probe with $\theta_a = 7.2°$ used under these conditions underestimates the fluence rate; the probes with $\theta_a = 15.1°$ and $\theta_a = 21.2°$ that have acceptance angles exceeding the band size

Table 2. Processed and Nonprocessed Fluence Rate Values $I(P)$[a]

Probe Parameters	Nonprocessed Results: Equidistant Measurements[b] S	Δ	K	$I(P)$	Constant Geometry[c] ($S = 0.0954$) $I(P)$	Processed Results: Constant Geometry[c] $I(P)$
$m = 44.23$, $\theta_a = 7.2°$	0.0538	15°	13	466.9	274.2	351.0
$m = 20$, $\theta_a = 10.7°$	0.0954	20°	10	581.8	581.8	350.6
$m = 10$, $\theta_a = 15.1°$	0.2141	30°	7	520.8	1165.0	350.5
$m = 5$, $\theta_a = 21.2°$	0.4783	45°	5	462.2	2308.2	350.9

[a]These values are obtained from the same sets of measured fluxes M_i as used in Table 1. S is the reference area of the probe; $\Delta \approx 2\theta_a$ is the step between measurements; K is the number of measurements. The true value of $I(P)$ is 349.9 relative units.
[b]Geometry is adjusted to the band size.
[c]Here $\Delta = 20°$ and $K = 10$.

highly overestimate it. Column 7 of Table 2 describes the same measurements as column 6, with the difference that the data were processed by the theory. The estimates in column 7 are very precise, with deviations from the true value within 1%, independent of whether the band size is adjusted to the acceptance angle of the probe (line 2) or not (lines 1, 3, and 4).

Appendix A: Geometry of Ellipses S_{ij}

We consider the measurement θ_i and the corresponding circular disk S_i normal to the direction $\theta = \theta_i$. The circumference $\theta = \bar{\theta}_j$ on the unit sphere is mapped onto the plane S_i as the ellipse S_{ij}. Let us designate the half-axes of S_{ij} as a_{ij}, b_{ij} and the x coordinate of the center as q_{ij} (see Fig. 9). As we can easily see from Fig. 9,

$$
\begin{aligned}
a_{ij} &= \sin\bar{\theta}_j \cos\theta_i,\\
b_{ij} &= \sin\bar{\theta}_j,\\
q_{ij} &= \cos\bar{\theta}_j \sin\theta_i,\\
c_{ij}^{\,2} &= b_{ij}^{\,2} - a_{ij}^{\,2} = \sin^2\bar{\theta}_j \sin^2\theta_i. \qquad \text{(A1)}
\end{aligned}
$$

The equation of the ellipse S_{ij} in the polar coordinates (r, φ) is given by expressions (see the appendix in Ref. 10) $r = f_{ij}^{\,+}(\varphi)$ when point P is inside S_{ij} and $r = f_{ij}^{\,\pm}(\varphi)$ when point P is outside S_{ij}, where

$$
f_{ij}^{\,\pm} = \frac{q_{ij}b_{ij}^{\,2}\cos(\varphi) \pm a_{ij}b_{ij}[a_{ij}^{\,2} - q_{ij}^{\,2} + (q_{ij}^{\,2} + c_{ij}^{\,2})\cos^2(\varphi)]^{1/2}}{a_{ij}^{\,2} + c^2\cos^2(\varphi)}. \qquad \text{(A2)}
$$

Substituting Eq. (A1) into Eq. (A2), we obtain

$$
f_{ij}^{\,\pm}(\varphi) = \frac{\cos\bar{\theta}_j \sin\theta_i \cos\varphi \pm \cos\theta_i[\sin(\theta_i + \theta_j)\sin(\theta_j - \theta_i) + \sin^2\theta_i\cos^2\varphi]^{1/2}}{\cos^2\theta_i + \sin^2\theta_i\cos^2\varphi}. \qquad \text{(A3)}
$$

Point P is located inside the ellipse S_{ij} when $a_{ij}^{\,2} - q_{ij}^{\,2} > 0$, which yields the condition $\sin(\theta_i + \bar{\theta}_j)\sin(\bar{\theta}_j - \theta_i) > 0$, i.e., $\pi - \theta_i > \bar{\theta}_j > \theta_i$. Outside the range where this condition holds the inequality $\sin(\theta_i + \bar{\theta}_j)\sin(\theta_i - \bar{\theta}_j) > 0$ is valid.

Let us consider the area $\theta_i > \bar{\theta}_j$, i.e., the case in which the ellipse S_{ij} is completely on the positive semiaxis x. We draw a tangent to the ellipse S_{ij} from point P. The coordinate of the point of tangency $\bar{\varphi}_{ij}$ is found from the condition for vanishing of the radical in Eq. (A3): $\sin(\theta_i + \bar{\theta}_j)\sin(\bar{\theta}_j - \theta_i) + \sin^2\theta_i\cos^2\varphi = 0$, which yields

$$
\cos\bar{\varphi}_{ij} = \frac{[\sin(\theta_i + \bar{\theta}_j)\sin(\theta_i - \bar{\theta}_j)]^{1/2}}{\sin\theta_i}.
$$

If the ellipse S_{ij} has a point of contact with disk S_i, its coordinate $\varphi = \varphi_{ij}$ is found from the condition $f_{ij}^{\,+} = 1$, which holds when $\cos\varphi_{ij} = \cos\bar{\theta}_j/\sin\theta_i$.

Appendix B: Calculation of integrals J_{i1}

This calculation is of integrals J_{i1} when the collimated component is presented as a singularity by means of a δ function. The collimated component of radiance F_c can be presented as $F_c = F_p\,\delta(\mu - 1)$, where

F_p is the collimated flux at point P,
$\mu = \cos\theta$,
$\int_0^1 \delta(\mu - 1)d\mu = 1$,
$\int_0^1 f(\mu)\delta(\mu - 1)d\mu = f(1)$.

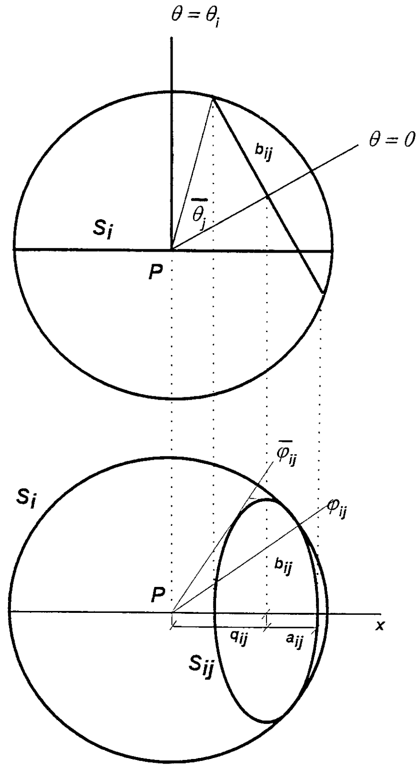

Fig. 9. Derivation of formulas for the half-axes a_{ij}, b_{ij} of the ellipse S_{ij} and the distance q_{ij} between the point P and the center of S_{ij}. All designations are the same as in Figs. 3, 5, and 7. The top section shows the vertical cross section of the unit sphere containing the directions $\theta = 0$ and $\theta = \theta_i$. The bottom section shows the cross section of the unit sphere through the plane xPy normal to the direction $\theta = \theta_i$.

For a measurement in the direction $\theta_i \leq 90°$, one should specify

$$L_1 = F_p,$$
$$J_{i1} = \int_0^1 h(\upsilon)\delta(\mu - 1)\mathrm{d}\mu.$$

For $h(\upsilon) = \cos \upsilon \exp(-m \sin^2 \upsilon)$ we obtain

$$\upsilon = \theta - \theta_i,$$
$$\cos \upsilon = \mu \cos \theta_i + \sqrt{1 - \mu^2} \sin \theta_i,$$
$$\sin \upsilon = \sqrt{1 - \mu^2} \cos \theta_i - \mu \sin \theta_i,$$
$$J_{i1} = \cos \theta_i \exp(-m \sin^2 \theta_i).$$

This research was supported by grant Fu 152/6-2 from Deutsche Forschungs-gemeinschaft, the Max-Planck Gesellschaft, and the Carlsberg foundation, Denmark (for B. Jørgensen). This paper is dedicated to P-S. Song on the occasion of his 60th birthday.

References and Notes

1. T. C. Vogelmann and L. O. Björn, "Measurements of light gradients and spectral regime in plant tissue with a fiber optic probe," Physiol. Plant. **60,** 361–368 (1984).
2. B. B. Jørgensen and D. J. Des Marais, "A simple fiber-optic microprobe for high resolution light measurements: application in marine sediment," Limnol. Oceanogr. **31,** 1376–1383 (1986).
3. L. Lilge, T. Haw, and B. C. Wilson, "Miniature isotropic optical fibre probes for quantitative light dosimetry in tissues," Phys. Med. Biol. **38,** 215–230 (1987).
4. T. C. Vogelmann, G. Martin, G. Chen, and D. Buttry, "Fibre optic microprobes and measurement of the light microenvironment within plant tissues," Adv. Bot. Res. **18,** 255–295 (1991).
5. L. Fukshansky, N. Fukshansky-Kazarinova, and A. Martinez v. Remisowsky, "Estimation of optical parameters in a living tissue by solving the inverse problem of the multi-flux radiative transfer," Appl. Opt. **30,** 3145–3153 (1991).
6. M. Kühl and B. B. Jørgensen, "Spectral light measurements in microbenthic communities with a fiber-optic microprobe coupled to a sensitive diode array detector system," Limnol. Oceanogr. **37,** 1813–1823 (1992).
7. M. Kühl and B. B. Jørgensen, "The light field of microbenthic communities: radiance distribution and microscale optics of sandy coastal sediments," Limnol. Oceanogr. **39,** 1368–1398 (1994).
8. M. Kühl, C. Lassen, and B. B. Jørgensen, "Optical properties of microbial mats: light measurements with fiber-optic microprobes," in *Microbial mats: Structure, Development and Environmental Significance*, L. J. Stal and P. Gaumette, eds., NATO ASI Series G (Springer-Verlag, Berlin, 1994), pp. 149–166.
9. T. Richter and L. Fukshansky, "Optics of bifacial leaf: 1. A novel procedure for derivation of the optical parameters," J. Photochem. Photobiol. **63,** 507–516 (1996).
10. N. Fukshansky-Kazarinova, L. Fukshansky, M. Kühl, and B. B. Jørgensen, "Theory of equidistant three-dimensional radiance measurements with optical microprobes," Appl. Opt. **35,** 65–73 (1995).
11. J. M. Senior, *Optical Fiber Communications: Principles and Practice* (Prentice-Hall, Englewood Cliffs, N.J., 1985).
12. By calibrating the microprobe against a standard source, we can express the measured values in absolute units of W m^{-2} s^{-1} sr^{-1} for L_i and W m^{-2} s^{-1} for $I(P)$. However, this is not necessary for our purposes.